Tension and Torsion Sensing With a Double-Taper Mach-Zehnder Interferometer

Pourya Ghasemi [ID], *Graduate Student Member, IEEE*, and Scott S.-H. Yam [ID], *Member, IEEE, Member, OSA*

Abstract—A novel setup for a Double-Taper Mach-Zehnder Interferometer (DTMZI) is presented to measure axial strain and torsion. An epoxy section is added between the two tapers as a fixture to ensure torsion sensing. The modal filtering effect of the epoxy upon the interferometry response is experimentally verified. The transmission spectrum of DTMZI under strain and torsion is modelled and further analyzed through the differential accumulated phase between the beating modes. The experimental spectral observation confirms our estimate. The relationships between the spectral shifts in wavelength and applied displacements are obtained. The sensor shows a very high sensitivity against the applied strain and twists.

Index Terms—Abrupt taper, strain sensing, torsion, tension, coupling, interferometry, single-mode fiber.

I. INTRODUCTION

FIBER optic sensors have been used in a variety of applications measuring such mechanical parameters as strain and torsion [1]. Several methods have been used to design a fiber optic sensor based on modal interferometry. Examples include Multimode fibers (MMFs) [2], Fiber Bragg Gratings (FBGs) [3], Long Period Gratings (LPGs) [4], multicore fibers [5], Photonic Crystal Fibers (PCFs) [6], and in-line fiber tapers [7] are those waveguides providing such conditions. Amongst all, the latter in the form of a Double-Taper Mach-Zehnder Interferometer (DTMZI) shows more promise as it can be fabricated quickly with the essential tools in hand, namely single-mode fiber (SMF) and fusion splicer [8]. Moreover, abrupt taper's modeling and its fabrication imperfections have been thoroughly investigated via recent works [9]–[11]. The application of measuring axial strain has been studied on DTMZI, and their modal behaviour has been thoroughly studied [12], [13]. Besides, several reports show the versatility of DTMZI sensors in such applications as refractive index (RI) and temperature sensing [14]–[16]. Although a combination of a pre-twisted fiber taper and MMF has been studied to measure torsion [2], there has been no report of DTMZI performance to measure twists and torsion using only a single-mode fiber.

This paper demonstrates a new setup for a DTMZI that ables the sensor to measure the two targeted mechanical parameters: axial strain and twist. The measurement of twist can only be executable with one of the taper's fixed. In our setup, we have added an epoxy section between the two tapers to fix the position of one taper and apply displacement on the other, demonstrated in Fig. 1(a). Further, the epoxy section introduces a modal filtering effect that is included in our modelling. Initially, utilizing the coupled-mode theory (CMT), we studied the analytical behaviour of DTMZI under these mechanical forces and provided parameters for further modelling and simulation. Next, the spectral behaviour of DTMZI under tension and torsion is modelled. Through our experimental studies, the modal filtering effect of the epoxy is confirmed to meet our simulation assumptions. The interferometric spectral peaks and dips shift with applied strain or torsional forces. The relation between the wavelength shifts and mechanical parameters is experimentally studied. The experimental results show an agreement between our modelling estimate and spectral observations.

II. THEORY

A DTMZI is configured with two in-line tapers, shown in Fig. 1(b), one of which is responsible for the higher-order modes (HOMs) excitation (the left taper), while the other taper acts as a phase-matching component to form interferometry between the HOMs and the fundamental mode. Based on the taper's geometry and the RI contrast of the SMF, the modes' excitation order and power evolution can be calculated using the CMT [11], [17]–[20]. The power evolution calculation provides us with a set of linearly polarized (LP) modes $\{\Psi_\nu\}$, their Effective Refractive Indices (ERIs) $\{n_\nu\}$, and complex amplitudes $\{A_\nu\}$ along each taper; ν is the mode index.

Given identically fabricated tapers, at wavelength λ, the constructive or destructive interferometry occurs between those modes with a total accumulated differential phase of $\pm q\pi$; q is an integer [13]. The total accumulated differential phase for each mode ν can be estimated through the following:

$$\Phi_\nu = \omega\tau_\nu + \Delta\phi_{\nu,01}, \qquad (1)$$

where ω is $2\pi c/\lambda$; with c as the speed of light and λ as wavelength. $\tau_\nu = (n_\nu - n_{01})\frac{L_i}{c}$ is the relative time-delay difference between the mode ν and LP$_{01}$ and L_i is the interferometry length. The term $\Delta\phi_{\nu,01} = \phi_\nu - \phi_{01}$ denotes the total differential phase accumulation along the tapers between mode ν and LP$_{01}$. Each mode's accumulative phase along two tapers can be
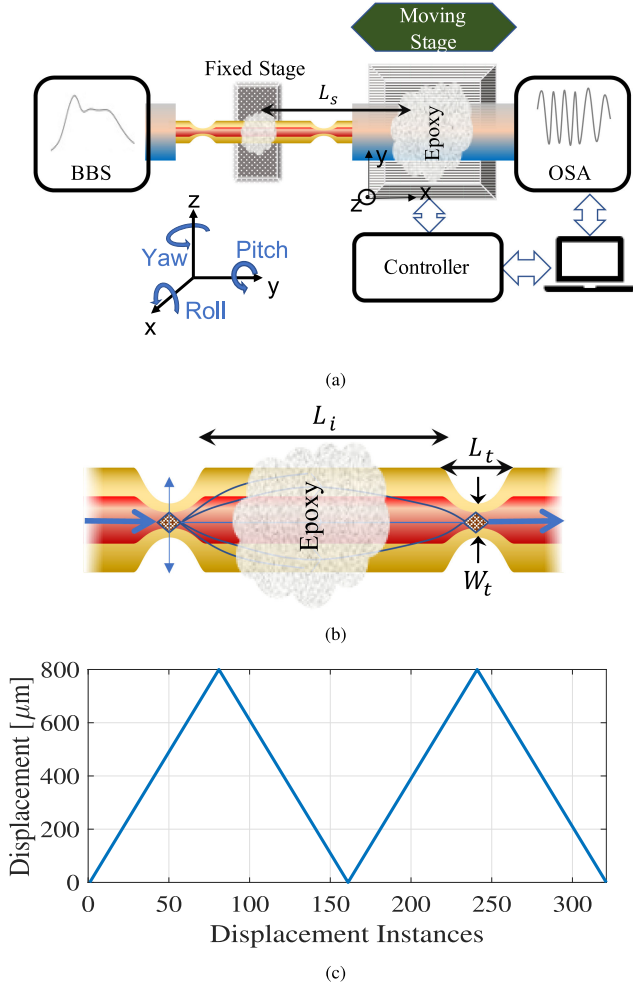
(a)

(b)

(c)

Fig. 1. (a) Experimental setup for testing strain, torsion, and bending with BBS and OSA at transmitter and receiver sides. The length L_s denotes the section of fiber between the fixtures which goes under load. (b) DTMZI with interferometry length of L_i comprising two identical tapers each with length of L_t and waist diameter of W_t, (c) the feedback reference displacement vector.

represented as:

$$\phi_\nu = 2 \times k_0 \int_0^{L_t} n_\nu(x')dx', \qquad (2)$$

with L_t as the length of the taper, and n_ν as the mode's ERI along the taper.

Assuming each mode's complex amplitude as $\{a_\nu \exp(i\phi_\nu)\}$, the power spectral density can be simulated as the following, demonstrating the spectrum's dependence upon the ERIs' differences in terms of time-delays between the modes:

$$\Gamma(\omega) = |a_{01}|^2 \left(1 + \sum_\nu \frac{|a_\nu|^2}{|a_{01}|^2}\right.$$
$$+ \sum_\nu 2\frac{|a_\nu|}{|a_{01}|}\cos(\omega\tau_\nu + \Delta\phi_{\nu,01})$$
$$\left.+ \sum_{\nu>\mu} 2\frac{|a_\nu a_\mu|}{|a_{01}|^2}\cos(\omega\Delta\tau_{\nu,\mu} + \Delta\phi_{\nu,\mu})\right),$$
$$(3)$$

with $\Delta\phi_{\nu,\mu} = \phi_\nu - \phi_\mu$, $\Delta\tau_{\nu,\mu} = \tau_\nu - \tau_\mu$. The first two terms $(1 + \sum_\nu \frac{|a_\nu|^2}{|a_{01}|^2})$ corresponds to the average power of the modes. The third term interprets the beatings between the HOMs and the LP_{01} mode. Moreover, the last term represents the reverberations between the HOMs. In our setup, as shown in Fig. 1, we have used epoxy as a fixture between the two tapers, with an RI greater than the cladding, which in turn dissipates some of HOMs and only lower order modes will survive to join the interferometry at the second taper. This limits the second term to the first five modes, causes the last term to vanish. Thus, (3) can be simplified as:

$$\Gamma(\omega) \approx I_{dc} + \sum_{\nu=02}^{05} I_{ac,\nu} \cos(\omega\tau_\nu + \Delta\phi_{\nu,01}), \qquad (4)$$

where $I_{dc} = \sum_{\nu=01}^{05} |a_\nu|^2$ is the average intensity, and $I_{ac,\nu} = 2|a_{01}a_\nu|$ is the sinusoidal intensity associated with νth mode.

By applying a tensile, torsional, or shear force at one end of the DTMZI the cosine argument of the (4) will change due to the alterations upon the differential group-delay τ_ν and $\Delta\phi_{\nu,01}$.

A. Stretching on the X-Axis

As the fiber is stretched along the x-axis, the tensile forces are causing the elongation in the interferometry length (L_i) which changes τ_ν to $\tau_\nu(1 + \alpha\varepsilon_x)$, with $\varepsilon_x = \frac{\Delta L}{L_s}$ as the strain, $\alpha = \frac{L_s}{L_i}$ as the relative length coefficient, and L_s as the total length under strain. Also, $\Delta\phi_{\nu,01}$ changes according to the elongation in the taper's length (L_t) meaning an extension on the upper limit of integral in (2) along with alterations on ERIs:

$$\Delta\phi_{\nu,01}(\varepsilon_x) = \Delta\phi_{\nu,01}^{T_1}$$
$$+ k_0 \int_0^{L_t+\Delta L} (\tilde{n}_\nu(x';\varepsilon_x) - \tilde{n}_{01}(x';\varepsilon_x))dx',$$
$$(5)$$

where the first term is associated with the accumulated phase on the first taper free of any tension: $\Delta\phi_{\nu,01}^{T_1} = k_0 \int_0^{L_t}(n_\nu(x') - n_{01}(x'))dx'$, and the second term denotes the accumulated phase upon the second taper under strain. Also, the new ERIs $\{\tilde{n}_\nu\}$ for the second taper differ from the initial set of ERIs $\{n_\nu\}$ following the stretched geometry of the second taper. So, the Eq. (4) can now be modified as the following to reflect the elongation effect:

$$\Gamma(\omega; \varepsilon_x)$$
$$\approx I_{dc} + \sum_{\nu=02}^{05} I_{ac,\nu} \cos(\omega\tau_\nu(1 + \alpha\varepsilon_x) + \Delta\phi_{\nu,01}(\varepsilon_x)). \quad (6)$$

B. Twists on Roll-Axis

Twisting the fiber results in an unbalanced stretching situation where the cladding is stretched more than the core due to the linear distribution of shear stress across the radius of a fiber under torsion. A more stretched cladding has a lower refractive index which leads to a higher RI contrast between cladding and core. The more contrast between the core-cladding RI the more contrast between the ERI of the modes, therefore, the differential

phase will alter as:

$$\Delta\phi_{\nu,01}(\varepsilon_R) = \Delta\phi_{\nu,01}^{T_1}$$
$$+ k_0 \int_0^{L_t} (\tilde{n}_\nu(x';\varepsilon_R) - \tilde{n}_{01}(x';\varepsilon_R))dx'. \quad (7)$$

where the second term denotes the accumulated phase upon the second taper under torsion, with modified ERIs as $\{\tilde{n}_\nu\}$. The term $\varepsilon_R \approx \Delta_R/r_{cl}$ represents the angle of twist as a result of applying a displacement of Δ_R on the roll-axis [21], while r_{cl} is the cladding's radius. It is to note that the cladding's radius varies along the taper, hence, the gradient of the rotation vector along the x-axis varies which projects in terms of strain along the x-axis [22]. Therefore, the transmission spectrum can now be formulated as:

$$\Gamma(\omega;\varepsilon_R,\varepsilon_{R,x}) \approx I_{dc}$$
$$+ \sum_{\nu=02}^{05} (I_{ac,\nu}\cos(\omega\tau_\nu(1+\alpha'\varepsilon_{R,x}) + \Delta\phi_{\nu,01}(\varepsilon_R))), \quad (8)$$

where $\varepsilon_{R,x} = \frac{\Delta_R}{2}\int_0^{L_t}|\frac{\partial}{\partial x}(\frac{1}{r_{cl}(x)})|dx$ is the strain applied upon the x-axis as a result of the rotation, and $\alpha' = \frac{L_t}{L_i}$ is the relative length coefficient. The tapering outline for the cladding's radius is formulated as:

$$r_{cl}(x) = \frac{1}{2}\left[(r_{cl_1} + r_{cl_2}) + (r_{cl_1} - r_{cl_2})\cos\left(2\pi\frac{x}{L_t}\right)\right], \quad (9)$$

where r_{cl_1} and r_{cl_2} are the cladding's radii at the bare section and tapered waist, respectively. So, the resultant strain upon x-axis regarding the applied rotation of Δ_R can approximated as:

$$\varepsilon_{R,x} \approx \frac{2\Delta_R}{r_{cl_1} + r_{cl_2}}\left(\frac{r_{cl_1} - r_{cl_2}}{r_{cl_1} + r_{cl_2}}\right), \quad (10)$$

which linearly rises with the applied rotation (Δ_R).

III. SIMULATION RESULTS

Each taper is fabricated on an SMF-28 with a core and cladding radius of 4.2 and 62.5 μm. The RIs core and cladding are given as 1.455 and 1.45, respectively, maintaining an RI step-index difference of $\Delta_n = 0.005$. Cladding's radius at the bare section and the tapered waist are $r_{cl_1} = 62.5$ μm and $r_{cl_2} = \frac{W_t}{2} = 20$ μm respectively. The core-cladding ratio is assumed the same along each taper: $r_{co}(x) = \frac{8.4}{125}r_{cl}(x)$. The taper's length $L_t = 700$ μm. The x-axis segmentation element is set to $\Delta_x = 1$ μm.

The tapered sections are more prone to reflect via tensile, torsional, or bending, due to their higher flexibility and delicacy compared with the bare fiber. So, the displacements are assumed to distribute evenly on the second taper, located on the OSA side in Fig. 1.

A. Excitation and Radiation

The first taper is initially excited with LP$_{01}$, and at the output, it excites HOMs with LP$_{05}$ mode as the most prior in power [9]. The refractive index of the epoxy layer is assumed to be 1.467,
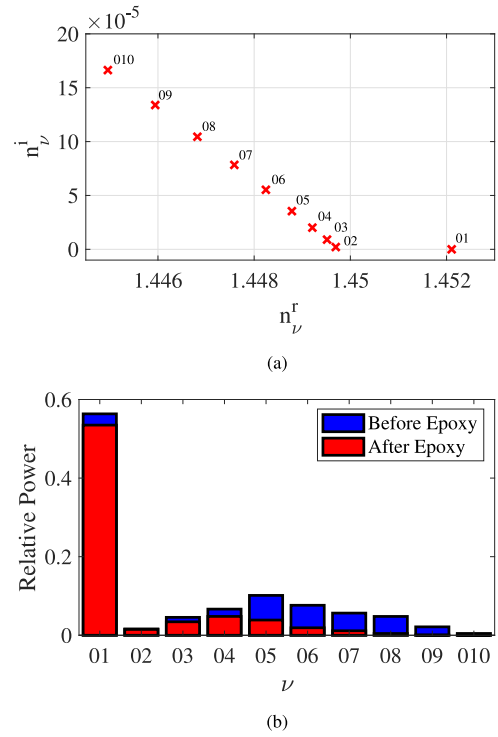

Fig. 2. (a) Real and imaginary parts of the HOMs' ERI, (b) The effect of epoxy section upon the mode's power priority and dissipation.

which causes the ERI of the coupled modes to attain an imaginary part leading to the HOMs dissipation and change in priority order. The ERI of the HOMs at the epoxy section is illustrated in Fig. 2(a), where the imaginary part of the modes' ERI increases linearly with the order of the HOM while it remains negligible for the fundamental mode. The mode excitation effect of the epoxy section is depicted in Fig. 2(b). Before the epoxy section, the most dominant HOM is LP$_{05}$ and the HOMs continuum last to LP$_{010}$, but after the epoxy is applied, the most dominant mode will appear as LP$_{04}$ while LP$_{09}$ and LP$_{010}$ are entirely dissipated. In the following discussions, we will focus on the behaviour of the four most predominant HOMs, being LP$_{02}$, LP$_{03}$, LP$_{04}$, and LP$_{05}$.

B. Displacements on X-Axis

Upon applying strain, the second taper gets stretched, introducing alterations on the phase of the HOMs, as discussed through (5) and (6). Once the phase changes are introduced, the amplitude of the interferometry will also vary with the changes introduced into the phase-matching condition. The phase and amplitude of the HOMs, LP$_{0m}$; $m = 2\ldots5$, versus applied strain is studied in Fig. 3 at $\lambda = 1550$ nm. As it is shown, the differential accumulative phase of each mode varies linearly with applied displacements. The variation rate of $\Delta\phi_{01,\nu}$ increases by the order ν, for instance, the absolute total change of phase for $\nu = 02, 03, 04, 05$ are $\frac{\pi}{2}, \pi, \frac{3\pi}{2}, 2\pi$, respectively. The combined intensity $I_{ac,\nu}$ for LP$_{03}$ and LP$_{05}$ is fluctuating while gently increasing. For LP$_{04}$, $I_{ac,\nu}$ meets its minimum half way and

Fig. 3. The variations of interferometry's alternative intensity(left) and accumulative phase(right) components for the HOMs, LP_{02}, LP_{03}, LP_{04}, and LP_{05}, versus the displacements on x-axis.
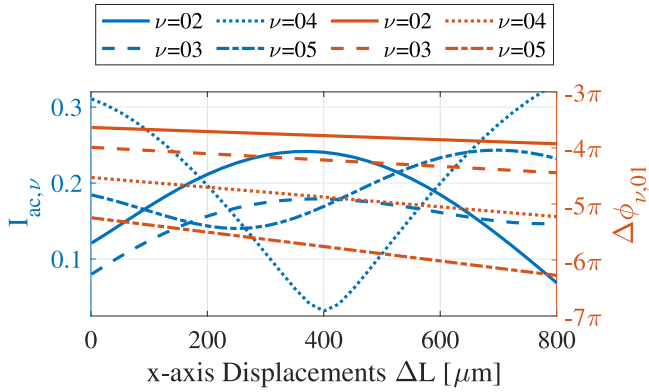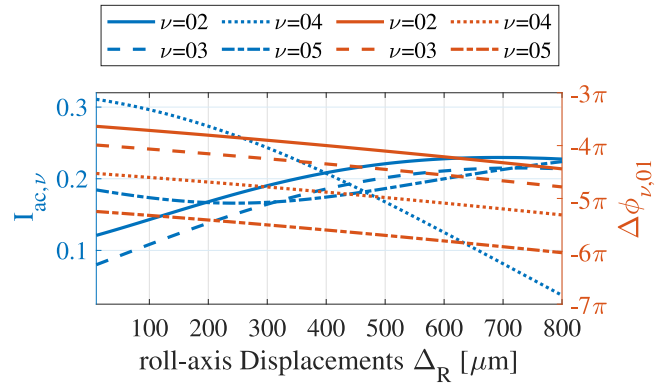

Fig. 5. The variations of interferometry's alternative intensity(left) and accumulative phase(right) components for the HOMs, LP_{0m}; $m = 2\ldots5$, versus the displacements on roll-axis.
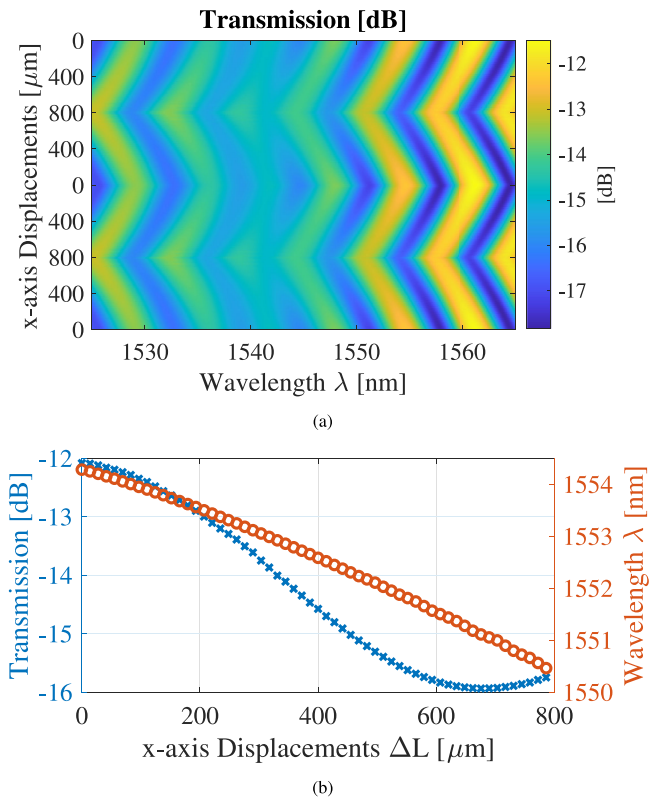

(a)

(b)

Fig. 4. (a) Simulated spectral signature of two cycles of applying strain to the DTMZI, (b) track of a sample peak's transmission and wavelength shift versus x-displacements.

rises to its initial value. In contrast, $I_{ac,\nu}$ for LP_{02} reaches its maximum around 380 μm and then decays to its minimum value.

The spectral signature for the DTMZI sensor under two cycles of applied strain is depicted in Fig. 4(a) where the interferometry peaks and dips are shifting to the lower wavelengths as displacements are increasing. In Fig. 4(b) the intensity and wavelength track of an interferometry peak starting at 1555 nm is depicted. It is to note that while the interferometry peak is shifting towards the lower wavelengths, its intensity is decreasing, which demonstrates the change in contrast between the relative amplitude of the modes as strain is applied.

C. Displacements on Roll-Axis

Displacements on the roll-axis translates to torsional forces upon the second taper causing a change in the boundary conditions regarding the increments in the RI difference: Δ_n. A higher RI contrast between core and cladding helps the light to remain more confined to the fundamental mode. Therefore, the amplitude of LP_{01} rises, while the amplitude of other HOMs is decreasing. Also, the HOMs' amplitude declination rate is relative to the mode's order, such that the higher the order, the less it gains power in the coupling process. In Fig. 5(left), the alternating intensity of the transmission spectrum for each mode ($I_{ac,\nu}$) is plotted against the displacements on roll-axis. As it is shown, the alternating intensity of early HOMs, $I_{ac,\nu}$; $\nu = 2, 3$, are increasing as they are multiplied by the increasing amplitude of the fundamental mode (a_{01}). As the order of mode is rising, the increasing rate in $I_{ac,\nu}$ fades, so that for LP_{05} the alternative intensity remains almost flat against the displacements on roll-axis, meaning the increment in a_{01} cancels out the decrement in a_{05}. Also, the LP_{04}'s amplitude decays in a much higher rate than the increments on a_{01} so that $I_{ac,04}$ drastically fades out as torsion is applied.

According to Eq. (7), as rotation is applied, the core-cladding RI contrast increases, resulting in a higher contrast between the ERI of the modes. Consequently, the differential accumulative phase will linearly vary with the applied twists on the roll-axis, demonstrated in Fig. 5(right). Although in comparison with Fig. 3(right), the differential phase shift vs. tension is less than the case of torsion, the combined phase shift according to Eq. (8) is higher due to the longitudinal strain produced by rotation.

The transmission spectrum of the DTMZI is simulated for two cycles of applied torsion in Fig. 6(a). While, the track of wavelength shifts and intensity fluctuation for an interferometry peak is shown in Fig. 6(b). As it is demonstrated, and in comparison with Fig. 4, the rapid variations in phase not only result in a sharper shift of the interferometry response against wavelengths but also causes fluctuations in the peaks and dips of the interferometry pattern along with the shifting effect. Also, the higher confinement of light in the core results in a growing intensity as the displacements are ascending.
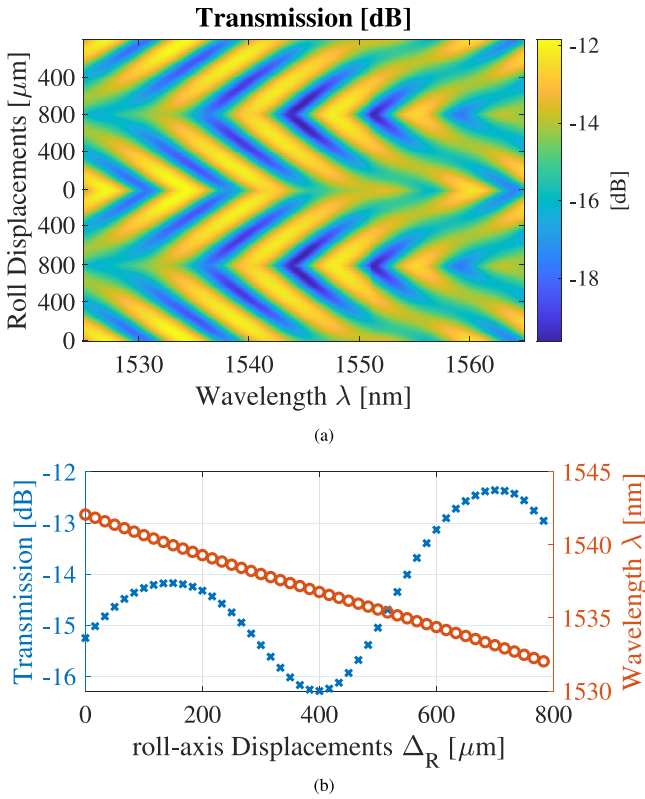
(a)

(b)

Fig. 6. (a) Simulated spectral signature of two cycles of applying twists to the DTMZI, (b) track of a sample peak's transmission and wavelength shift versus roll-displacements.

(a)

(b)

Fig. 7. The modal filtering effect of epoxy on the transmission spectrum (a), and its FFT (b).

IV. EXPERIMENTAL RESULTS AND ANALYSIS

As shown in Fig. 1(a), our experimental setup comprises a C-Band broadband fiber-optic source (BBS 1550 A-TS) at the transmitter side and an OSA for spectral observation. The two tapers are fabricated on an SMF-28 to form in-line modal interferometry. Each taper introduces a 3 dB loss upon the spectral power of the BBS. The interferometry length between the fabricated tapers (L_i) is set to 6 cm. The first taper acts as an excitation node for HOMs, and the second node provides the interferometry phase-matching condition between the copropagating modes. The sensor is fixed for strain sensing at two points such that only one of the tapers is under the influence of the displacements. The fiber's length under strain, or the initial distance between the fixed points is 20 cm. The HOMs excitation are estimated adopting the taper's modal decomposition technique introduced in [10].

A. Epoxy Modal Filtering Effect

The fixtures are made with a hot glue epoxy, the rigidity of which has been thoroughly tested after it sets. The hot glue epoxy provides the experimental procedure with flexibility, as it can be removed from the mounts and stages easily. Also, the use of epoxy in the interferometry length between the tapers shows a modal filtering effect in favour of repeatability and reproducibility. The modal filtering effect of the epoxy is depicted in Fig. 7. As shown after applying the epoxy on the
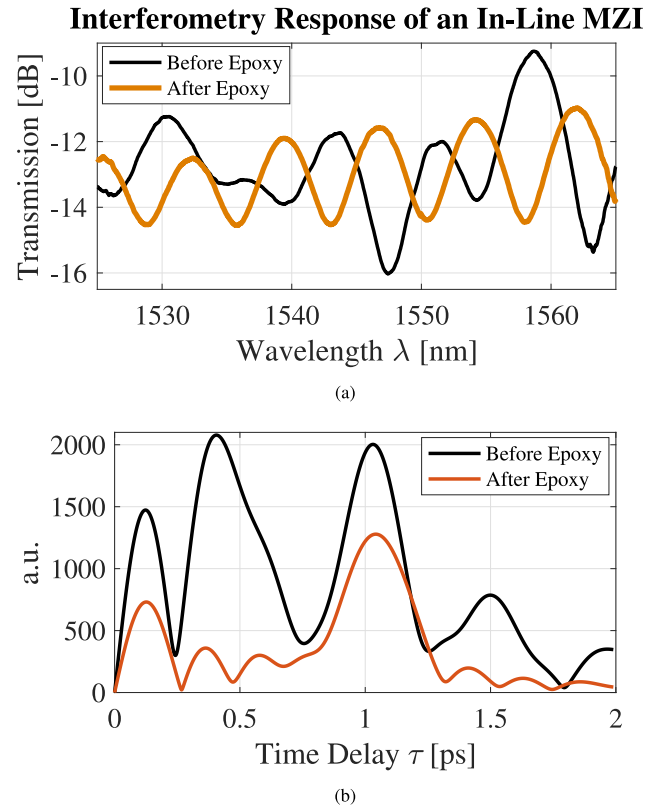
interferometry section between the tapers, mostly one of the HOMs remains beating with the fundamental mode. At the same time, the dominant frequency component of the interferometry response, corresponding to the beating between LP_{01} and LP_{05}, stays relatively the same before and after applying the epoxy, depicted in Fig. 7(b). However, due to the geometry of SMF, the ERI difference between the LP_{04} and LP_{05} modes are calculated in close vicinity: $|n_{05} - n_{04}| < 10^{-4}$. After the epoxy is applied, the HOMs are mostly dissipated and only the dominant HOMs, namely LP_{04} and LP_{05}, remain to beat with the fundamental mode, as simulation results suggest in Fig. 2. The combination of these two modes, regarding their close ERI and power, manifests as one dominant HOM that interferes with LP_{01}.

B. Strain Measurement on X-Axis

The strain test is accomplished by applying incremental displacements, with 10 μm steps, upon the x-axis. The test is designed to repeat for two cycles for repeatability confirmation. Also, fiber is set loose at the beginning state of the experiment to ease the calibration for the initial straining point. Fig. 8(a) demonstrates the experimental results regarding the strain sensing on the x-axis, where two cycles of strain are applied on the x-axis using the nano-positioners (Fig. 1(c)), and the spectral results are recorded. The spectral measurements on the x-axis show the spectral shifts with each displacement. The wavelength shifting and transmission variation trace for one of the interferometry's peaks versus the displacements is plotted
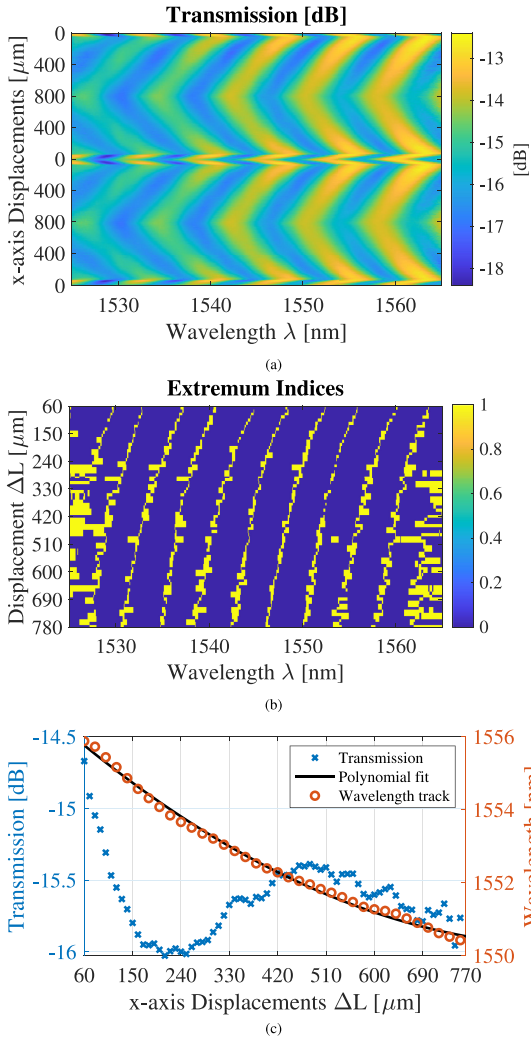
Fig. 8. (a) Transmission measurement for two cycles of applied strain, (b) Interferometry extremum index extraction for half a cycle of x-axis strain signature, (c) track of a sample peak's transmission and wavelength versus x-displacements.
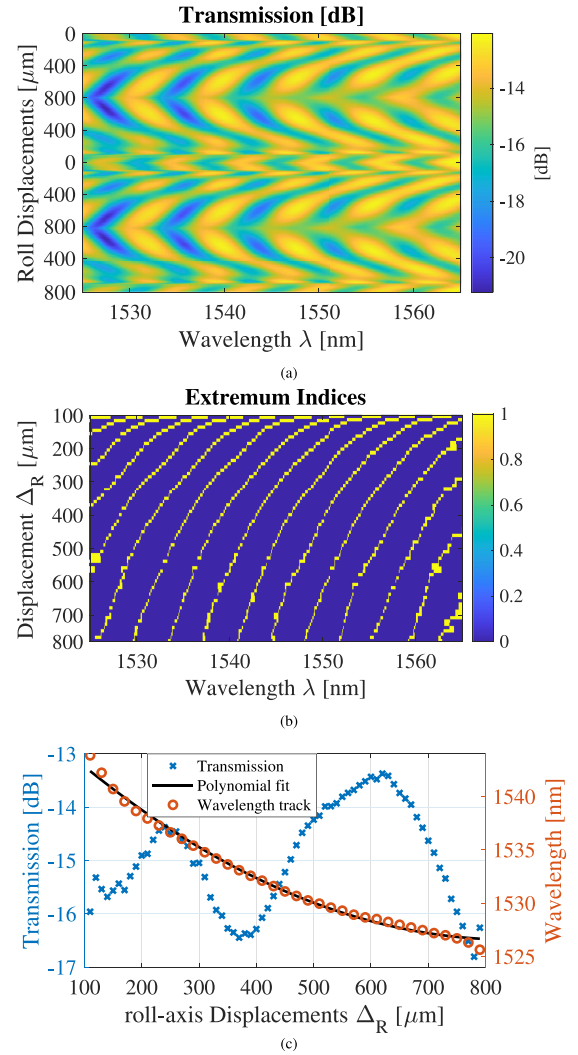

Fig. 9. (a) Transmission measurement for two cycles of applied torsion, (b) Interferometry extremum index extraction for half a cycle of roll-axis twisting signature, (c) track of a sample peak's transmission and wavelength versus roll-displacements.

in Fig. 8(c). As predicted through the simulation (Fig. 4), the interferometry peaks drop with applied strain due to the change in the second taper's geometry, resulting in an asymmetry in the DTMZI structure, causing a decrease in the amplitudes of HOMs (Fig. 3).

C. Twist Measurement on Roll-Axis

The transmission behaviour of our sensor under torsional forces is examined via rotational displacements upon the moving stage's roll-axis, with a step size of 10 μm. The interferometry response is recorded at each rotation from OSA (Fig. 9(a)). The repeatability of the process is ensured by repeating the process for two cycles of clockwise and counter-clockwise twists. The rotational displacement feedback is recorded from the nano-positioners and demonstrated in Fig. 1(c). The initial point where the taper starts to stretch occurs after a few displacements where the trend of the wavelength shifts reverses, where the interferometry peaks consistently start moving towards lower wavelengths.

The wavelength shifting and transmission variation trace for one of the interferometry's peaks is plotted against the displacements in Fig. 9(c). The intensity fluctuations of the shifting peaks match our prediction in Fig. 6 which is a result of HOMs' rapid phase variation, studied in Fig. 5(right)). Also, the peak-peak variation of transmission increases as the displacements arise associated with higher confinement of light in the core due to increased RI contrast between core and cladding.

D. Strain and Angle of Twist Versus Wavelength

The relation between the applied strain and torsion can be extracted by tracking each peak's wavelength. First, the initial point where the tension starts should be determined, which can be easily accomplished by tracking the change of trend in the wavelength shifts. Next, the peaks and dips of the interferometry signature at each displacement should be calculated. In order to avoid spectral background noise, interferometry responses

TABLE I
STRAIN AND TWIST FITTING CURVES

$Q = p_2\lambda^2 + p_1\lambda + p_0$; λ in [nm]			
Q	p_2	p_1	p_0
$\varepsilon_x : [\mu\varepsilon]$	212.6	-1148	1640
$\varepsilon_R : [rad]$	1.11	-5.335	7.142

should be filtered through a moving average process. The results of extracting the interferometry patterns' extremums are represented in Fig. 8(b) where each light square associates a one to the peak or dip wavelength. Fig. 8(b) is the wavelength trend extremum extraction related to the strain pattern in Fig. 8(a) for the uprising strain as half of its first cycle. Likewise, the wavelength trend extremum extraction related to the twisting pattern in Fig. 9(a) for the clockwise torsion as half of its first cycle is shown in Fig. 9(b). It is shown that the wavelength shifting trend stands the same for all of the extremums.

Once the extremum indices are extracted, the associated wavelengths can be extracted for each displacement. Then, the tracking of a change upon a selected wavelength will be accomplished by following the minimum squared error between the neighbouring instances of displacement. However, multiple minimization points can occur as a tracking error due to the gaps between the tracking points. Thus, it is essential to impose the continuity upon tracking a wavelength as it shifts from one instance to another. The results of the wavelength shift tracking process are demonstrated in Fig. 9(c)(right) and 8(c)(right), where extracted results are fitted with a second-order polynomial. The comparison between Fig. 9(c)(right) and 8(c)(right) shows a higher sensitivity of the device under a twisting load so that a peak's wavelength will shifts by 18 nm for 800 μm rotation on roll-axis (Δ_R), whereas for an applied strain on the x-axis with $\Delta_L = 800\mu m$ the total wavelength shift is less than 6 nm. The displacement vector at the horizontal axis of these plots can be mapped to the strain and the angle of twist using $\varepsilon_x = \Delta_L/L_s$ and $\varepsilon_R = \Delta_R/r_{cl}$. The polynomial fitting results after we apply the mappings on the horizontal axis are denoted in Table. I. The fitting results show a more strong dependency on the linear coefficient p_1 for both curves; hence, we can estimate the sensitivity of the tensile strain as 638.30 $\mu\varepsilon$/nm and the twist as 0.92 rad/nm.

V. CONCLUSION

A new setup for a DTMZI is demonstrated for the measurement of axial strain and twist. In favour of measuring twists, an epoxy section is added between the two tapers as a fixture which further introduces a modal filtering effect. The phase-matching criteria of the DTMZI sensors is studied. The spectral behaviour of DTMZI under strain and torsion is modelled and analyzed. The experimental results confirms our modelling estimate via spectral observations. The relations between peak/dip shifts in

wavelength and applied displacements are extracted. The sensor shows a high sensitivity against the applied strain and twists.

REFERENCES

[1] V. Budinski and D. Donlagic, "Fiber-optic sensors for measurements of torsion, twist and rotation: A review," *Sensors*, vol. 17, no. 3, p. 443, 2017, https://doi.org/10.3390/s17030443

[2] S. Duan *et al.*, "High sensitive torsion sensor based on cascaded pre-twisted taper and multi-mode fiber sheets," *IEEE Photon. Technol. Lett.*, vol. 31, no. 19, pp. 1588–1591, Oct. 2019.

[3] Y. Lu, C. Shen, D. Chen, J. Chu, Q. Wang, and X. Dong, "Highly sensitive twist sensor based on tilted fiber bragg grating of polarization-dependent properties," *Opt. Fiber Technol.*, vol. 20, no. 5, pp. 491–494, 2014.

[4] A. S. Nair, V. S. Kumar, and H. Joe, "Twist sensitivity of cladding-mode resonances and its cross-sensitivity to strain and temperature in a mechanically induced long-period fiber grating," *Fiber Integr. Opt.*, vol. 33, no. 5/6, pp. 347–359, 2014.

[5] P. Zu *et al.*, "A temperature-insensitive twist sensor by using low-birefringence photonic-crystal-fiber-based Sagnac interferometer," *IEEE Photon. Technol. Lett.*, vol. 23, no. 13, pp. 920–922, Jul. 2011.

[6] W. Chen, S. Lou, L. Wang, H. Zou, W. Lu, and S. Jian, "Highly sensitive torsion sensor based on sagnac interferometer using side-leakage photonic crystal fiber," *IEEE Photon. Technol. Lett.*, vol. 23, no. 21, pp. 1639–1641, Nov. 2011.

[7] Q. Zhou *et al.*, "Fiber torsion sensor based on a twist taper in polarization-maintaining fiber," *Opt. Exp.*, vol. 23, no. 18, pp. 23 877–23886, 2015.

[8] S. Korposh, S. W. James, S.-W. Lee, and R. P. Tatam, "Tapered optical fibre sensors: Current trends and future perspectives," *Sensors*, vol. 19, no. 10, 2019, Art. no. 2294.

[9] X. Leng, S. S.-H. Yam, and P. Ghasemi, "Error estimation in the analytical modeling of abrupt taper Mach-Zehnder interferometers," *OSA Continuum*, vol. 3, no. 11, pp. 3048–3060, 2020.

[10] P. Ghasemi and S. S. Yam, "Spectral modal decomposition of abrupt fiber tapers based on simulated annealing method," *J. Lightw. Technol.*, vol. 39, no. 12, pp. 4209–16, 2021.

[11] P. Ghasemi and S. S.-H. Yam, "Analytical and experimental study on a bent abrupt taper," *Opt. Exp.*, vol. 29, no. 1, pp. 82–94, 2021.

[12] Z. Tian and S. S.-H. Yam, "In-line abrupt taper optical fiber mach-zehnder interferometric strain sensor," *IEEE Photon. Technol. Lett.*, vol. 21, no. 3, pp. 161–163, Feb. 2009.

[13] P. Ghasemi and S. S.-H. Yam, "Single wavelength strain sensing based on double taper mach-zehnder interferometer," *IEEE J. Sel. Topics Quantum Electron.*, vol. 27, no. 6, pp. 1–7, Nov./Dec. 2021.

[14] Z. Tian *et al.*, "Refractive index sensing with mach-zehnder interferometer based on concatenating two single-mode fiber tapers," *IEEE Photon. Technol. Lett.*, vol. 20, no. 8, pp. 626–628, Apr. 2008.

[15] Z. Tian and S. S.-H. Yam, "In-line single-mode optical fiber interferometric refractive index sensors," *J. Lightw. Technol.*, vol. 27, no. 13, pp. 2296–2306, 2009.

[16] T. Chen, R. Chen, P. Lu, Q. Chen, and K. Chen, "Tapered fibre mach-zehnder interferometer for simultaneous measurement of liquid level and temperature," *Electron. Lett.*, vol. 47, no. 19, pp. 1093–1095, 2011.

[17] Z.-J. Zhang and W.-K. Shi, "Eigenvalue and field equations of three-layered uniaxial fibers and their applications to the characteristics of long-period fiber gratings with applied axial strain," *JOSA A*, vol. 22, no. 11, pp. 2516–2526, 2005.

[18] M. Monerie, "Propagation in doubly clad single-mode fibers," *IEEE Trans. Microw. Theory Techn.*, vol. 30, no. 4, pp. 381–388, Apr. 1982.

[19] D. Marcuse, "Mode conversion in optical fibers with monotonically increasing core radius," *J. Lightw. Technol.*, vol. 5, no. 1, pp. 125–133, 1987.

[20] F. Gonthier, A. Hénault, S. Lacroix, R. J. Black, and J. Bures, "Mode coupling in nonuniform fibers: Comparison between coupled-mode theory and finite-difference beam-propagation method simulations," *JOSA B*, vol. 8, no. 2, pp. 416–421, 1991.

[21] J. Bailey and J. Y. Sheikh-Ahmad, "Fundamental aspects of torsional loading," *ASM Handbook.*, vol. 8, pp. 139–144, 1985.

[22] W. S. Slaughter, *The Linearized Theory of Elasticity*. Berlin, Germany: Springer, 2012.